Available online at www.sciencedirect.com
SCIENCE DIRECT®
Microporous and Mesoporous Materials 84 (2005) 153–160
MICROPOROUS AND MESOPOROUS MATERIALS
www.elsevier.com/locate/micromeso

Iron oxide nanoparticles inside the MCM-41 channels: Study of the structural stability of the support

J.F. Bengoa, M.V. Cagnoli, N.G. Gallegos, A.M. Alvarez, L.V. Mogni, M.S. Moreno [1], S.G. Marchetti *

CINDECA, Fac. Cs. Exactas, Fac. Ingeniería, UNLP, CICBA, CONICET. Calle 47, No. 257 (1900) La Plata, Argentina

Received 16 January 2004; received in revised form 9 May 2005; accepted 9 May 2005
Available online 27 June 2005

Abstract

We report the synthesis of the MCM-41 mesoporous solid chosen as support of Fe nanoparticles, which yields a narrow distribution of oxide crystal sizes. MCM-41 was synthesized in two different ways, with and without pH adjustment during the synthesis process, and impregnated by different methods with iron salts. They were characterized by atomic absorption spectroscopy, N_2 adsorption, X-ray diffraction, Mössbauer spectroscopy, high-resolution scanning transmission electron microscopy equipped with a high-angle annular dark-field detector, high-resolution transmission electron microscopy and energy dispersive X-ray spectroscopy.

When the support was synthesized without pH adjustment the preparation steps of the supported system, the water destroys the regular structure of hexagonal channels of the mesoporous solid. The structure is preserved when the support is synthesized with pH adjustment during the synthesis process due to its higher pore-wall thickness. In addition, this system has a higher percentage of the iron oxide nanocrystals located inside the channels of the support.

Keywords: Mesoporous material; Fe/MCM-41; Iron oxide nanoparticles; Mössbauer spectroscopy; STEM-HAADF

1. Introduction

The heterogeneous catalytic reactions depending on the crystal size of the active phase are known as "structure sensitive reactions" [1]. The CO hydrogenation is an example of this kind of reactions. The activity and selectivity of supported Fe catalysts depend on the metallic crystal size [2]. In this way, our purpose is to look for a material with a narrow size distribution of Fe oxide crystals. This will allow us obtaining a catalyst with a narrow size distribution of metallic iron crystals after the reduction treatment.

It is well known that amorphous supports lead to a broad distribution of crystal sizes with a consequent loss of selectivity. On the other hand, using zeolitic supports such as ZSM-5 and zeolite Y, it is very difficult to "anchor" an important fraction of Fe oxide crystallites into their narrow pores [3]. When the crystals were located inside the channels in the preparation steps, they migrate to the external surface of the zeolite during the reduction step [4]. The challenge is to find a support that overcomes these problems.

The mesoporous MCM-41 solid belongs to the M41S mesoporous molecular sieve family [5], with a hexagonal arrangement of uniform channels of 15–100 Å diameter. Due to its very high surface area and its narrow size pore distribution [5], in principle MCM-41 seems to be a good support material for iron oxide particles to be used as catalyst in reactions such as ethanol hydrotreatment

* Corresponding author. Tel./fax: +542214210711.
E-mail address: march@quimica.unlp.edu.ar (S.G. Marchetti).
[1] Centro Atomico Bariloche, 8400—San Carlos de Bariloche, Argentina.

1387-1811/$ - see front matter © 2005 Elsevier Inc. All rights reserved.
doi:10.1016/j.micromeso.2005.05.018

or, after reduction, in hydrocarbon synthesis and other catalytic reactions. However, it was found that the MCM-41 structure can collapse when it is subjected to treatments with different metal salt solutions and/or temperatures [6].

The purpose of the present study is to obtain supported Fe crystals into the channels of the MCM-41, preserving its structural properties, and emphasizing the importance of the control of preparation steps and the quality (ordering degree and wall thickness) of the mesoporous material used as support. To this end we have prepared MCM-41 by two different methods and added iron in different ways.

2. Experimental

Two MCM-41 supports were synthesized. The solid named MCM-41(B) was synthesized according to Beck's recipe [5]: 40 g of water, 20.6 g of sodium silicate (26.1% SiO_2) and 1.2 g of sulfuric acid were mixed with stirring during 10 min. Then, we added 21.48 g of cetyltrimethylammonium bromide in 50.23 g of water and stirred the resulting gel for 0.5 h. Afterwards, 20 g of water were added to the gel. It was heated at 373 K for 144 h in a Teflon lined autoclave. The resulting solid was filtered, washed and dried in air at room temperature. It was then calcined at 813 K for 1 h in flowing N_2 (150 cm^3/min) followed by 6 h in flowing air (150 cm^3/min).

The other solid, called MCM-41(R), was prepared according to the methodology proposed by Ryoo and Kim [7]: a solution of 40 g of sodium silicate (26.1% SiO_2) and 74 g of water was prepared. This solution was slowly added to 38 ml of cetyltrimethylammonium chloride and 0.65 ml of NH_3 with vigorous stirring at room temperature. This mixture was heated in a polypropylene bottle, without stirring to 373 K for 24 h. Then, it was cooled to room temperature. The pH was adjusted to approximately 11 by drop wise addition of acetic acid with vigorous stirring. The reaction mixture was heated again to 373 K for 24 h. This procedure for pH adjustment and subsequent heating was repeated twice. The resulting solid was treated in the same way as it was described above for the MCM-41(B) obtention.

Four catalysts were obtained treating MCM-41(B) in the following ways:

Fe/MCM-41(B1): pore volume to incipient wetness (PVI) impregnation with $Fe(NO_3)_3 \cdot 9H_2O$ aqueous solution (pH = 0.5). The sample was dried at room temperature in atmospheric air, calcined in dry N_2 stream (60 cm^3/min) from 298 to 598 K at 0.2 K/min and kept at 598 K for 1 h.

Fe/MCM-41(B2): iron belonging to $Fe(NO_3)_3 \cdot 9H_2O$ solution was complexed with EDTA. Then, the pH was regulated to 7.6 with NaOH. The MCM-41(B) was impregnated by PVI method with this final solution. After drying in air in the same way as Fe/MCM-41(B1), the sample was calcined in dry air stream (60 cm^3/min) from 298 to 773 K at 0.2 K/min and kept at this temperature for 1 h.

Fe/MCM-41(B3): mechanical mixing of MCM-41(B) with $Fe(NO_3)_3 \cdot 9H_2O$ and, in order to melt the iron salt, a thermal treatment at 320 K was carried out. Afterwards, the solid was treated in the same conditions as sample Fe/MCM-41(B1).

Fe/MCM-41(B4): PVI impregnation with iron acetyl acetonate ($Fe(AcAc)_3$) solution in benzene. This sample was treated in the same way that Fe/MCM-41(B2) but the final temperature was 648 K.

The final calcination temperatures were chosen according to the different decomposition temperatures of the anions used.

The fifth catalyst, Fe/MCM-41(R), was prepared by PVI impregnation with $Fe(NO_3)_3 \cdot 9H_2O$ aqueous solution (pH = 0.5). The drying and calcination were carried out in the same conditions as samples Fe/MCM-41(B1) and Fe/MCM-41(B3).

A final Fe concentration of about 5% (w/w) was obtained in all solids. The samples were characterized by atomic absorption spectroscopy (AAS), N_2 adsorption (BET), X-ray diffraction (XRD), high-resolution transmission electron microscopy (HRTEM), high-resolution scanning transmission electron microscopy (STEM) equipped with a high-angle annular dark-field detector (HAADF), energy dispersive X-ray spectroscopy (EDS) and Mössbauer spectroscopy (MS) at 298 and 22 K. TEM observations were done using two different microscopes operated at 200 kV: a Philips CM200 and a Tecnai F20 equipped with a HAADF and X-ray detector. The Mössbauer spectra were obtained in transmission geometry with a 512-channel constant acceleration spectrometer. A source of ^{57}Co in Rh matrix of nominally 50 mCi was used. Velocity calibration was performed against a 6 μm-thick α-Fe foil. All isomer shifts (δ) mentioned in this paper are referred to this standard. The temperature between 22 and 298 K was varied using a Displex DE-202 Closed Cycle Cryogenic System.

The Mössbauer spectra were evaluated using a least-squares nonlinear computer fitting program with constraints. Lorentzian lines were considered with equal widths for each spectrum component. The spectra were folded to minimize geometric effects.

3. Results and discussion

The X-ray diffraction patterns of MCM-41(B), MCM-41(R) and the impregnated samples before and after calcination are shown in Figs. 1 and 2 respectively.

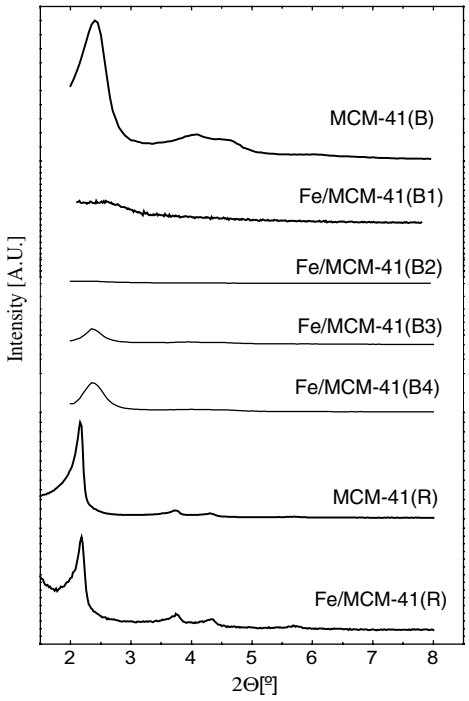

Fig. 1. X-ray diffraction patterns of MCM-41(B), MCM-41(R) and all the iron samples before calcination.

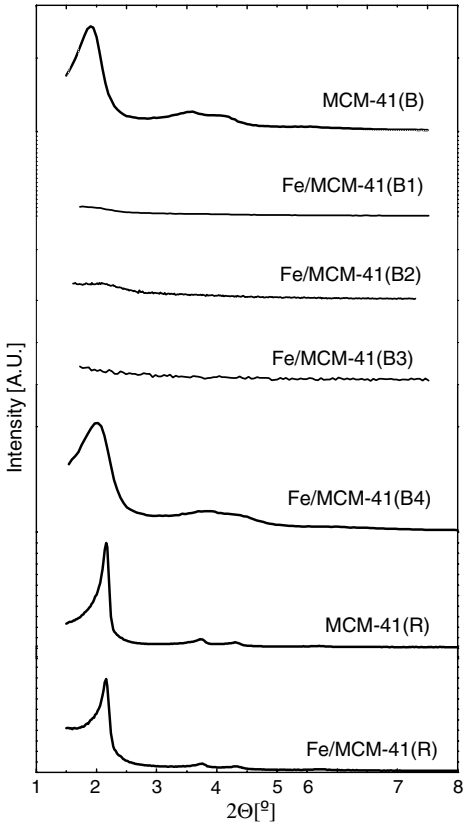

Fig. 2. X-ray diffraction patterns of MCM-41(B), MCM-41(R) and all the iron samples after calcination.

The supports show a different behavior when they were impregnated with $Fe(NO_3)_3 \cdot 9H_2O$ aqueous solution (pH = 0.5). The XRD patterns show that the Fe/MCM-41(B1) structure has collapsed before the calcination step, while Fe/MCM-41(R) has maintained it even after calcination. We can observe an increase of the peak intensity at $2\theta = 2.4^{\circ}$ of the calcined sample. This behavior could be attributed to the iron salt decomposition.

Fe/MCM-41(B2) showed the same behavior as Fe/MCM-41(B1). These results indicate that the pH of the impregnating solution is not responsible for the structure collapse and lead as to suppose that the structure destruction may be due to the water presence. It is probable that an hydrolytic attack on a Si–O–Si bond occurs. However, another possible explanation might be that, even at room temperature, the surface tension of the evaporating water causes collapse of the pores.

To eliminate the water present in the impregnation step we prepared Fe/MCM-41(B3). The XRD patterns show that the MCM-41(B) structure was preserved before calcination (Fig. 1). However, when the sample was calcined to carry out the anion decomposition, the structure fell down again (Fig. 2). We attribute this behavior to the water vapor presence belonging to the structural water of the iron salt. In this case, the surface tension of the evaporating water at the calcination temperature is the more likely mechanism to produce the structure collapse. Before calcination, this process is negligible since the structural water is not available to produce the material destruction through any mechanism.

According to the above results we impregnated MCM-41(B) with an iron salt without structural water, soluble in a non-polar organic solvent such as Fe $(AcAc)_3$ in benzene (Fe/MCM-41(B4)). This solid was able to maintain the mesoporous structure before and after the thermal treatment with an increase of the peak intensity at $2\theta = 2.4^{\circ}$ of the calcined samples in the same way as Fe/MCM-41(R). In this case, the solvent used has a much lower surface tension than water and its evaporation did not produce the structure collapse.

The different behavior of the two supports (MCM-41(B) and MCM-41(R)) during the impregnation and calcination steps led us to study why two solids that seem to be the same material must be treated in so different conditions to keep its structure. The above results called for a more exhaustive characterization of the two supports.

Table 1 shows the N_2 adsorption results of both supports. The specific surface area (S_g) and average pore radii (r_P) are similar in both samples (within the experimental error) and they are typical values for this family of mesoporous solids. Instead, the pore wall thickness of MCM-41(R) would be 40% higher than MCM-41(B). This value was obtained combining XRD and BET results, according to Beck et al. [5].

Table 1
Structural properties of MCM-41(B), MCM-41(R), Fe/MCM-41(B4) and Fe/ MCM-41(R)

Properties	MCM-41(B)		Fe/MCM-41(B4)	MCM-41(R)		Fe/MCM-41(R)
	BET	TEM	BET	BET	TEM	BET
S_g (m^2/g)	1148	–	1022	916	–	775
r_P (nm)	1.5	1.4	1.4	1.4	1.4	1.4
L (nm)	1.0	1.0	1.4	1.4	1.3	1.9
FHWM (nm)	–	0.70	–	–	0.53	–
N	–	379	–	–	59	–

S_g: Specific area. r_P: Average pore radii. L: Pore wall thickness. FHWM: Full width at half maximum of the pore distribution. N: Event numbers considered to obtain the pore distribution.

Some representative HRTEM images of the supports seen along and perpendicular to the pore axis are shown in Figs. 3 and 4. A hexagonal and regular array of uniform channels can be seen in both materials, with each pore surrounded by six neighbors. A more regular hexagonal arrangement of uniform pores at longer range is observed for MCM-41(R) with a thicker pore-wall.

Table 1 shows the average r_P and the pore-wall thickness (L) values obtained from statistical measurement from HRTEM images. The pore diameter distributions obtained from BET measurements and HRTEM images for both supports are compared in Fig. 5. There is a good agreement between the values obtained through both techniques. The broader pore radii distribution of MCM-41(B) (Table 1 and Fig. 5) confirms the lower regularity of its structure in comparison with MCM-41(R).

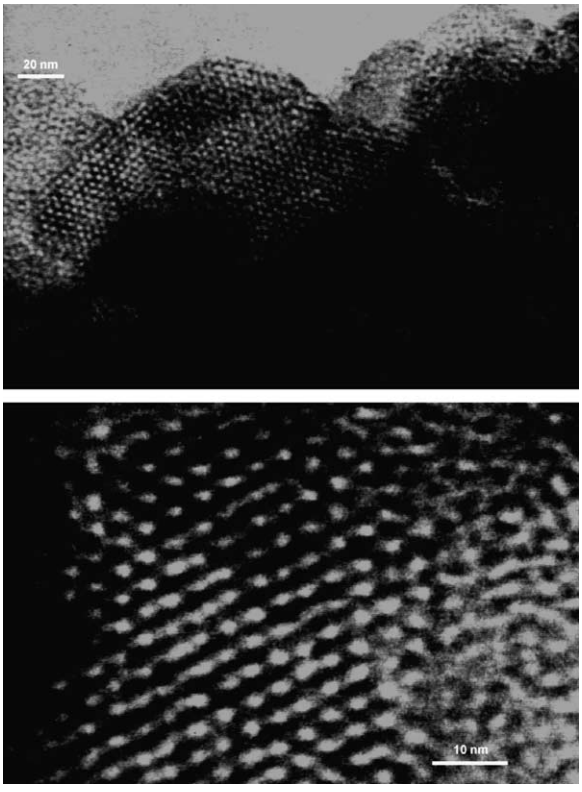

Fig. 3. HRTEM images of MCM-41(B).

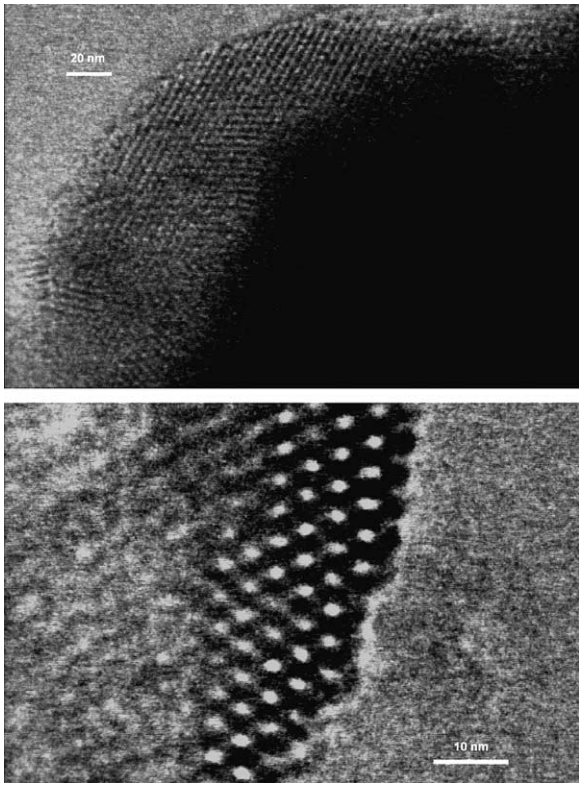

Fig. 4. HRTEM images of MCM-41(R).

It is necessary to remark that determination of pore wall thickness by BET, XRD and HRTEM could be subjected to an important error and the obtained values must be used only as a qualitative indication.

We can conclude that the better structural regularity and pore-wall thickness are responsible for the higher structural stability of MCM-41(R) during the preparation steps of the Fe/MCM-41 system. These results are in agreement with those reported by Kruk et al. [8].

Taking into account that just only Fe/MCM-41(B4) and Fe/MCM-41(R) have kept their structure after the preparation steps, a more exhaustive characterization was performed to identify the iron species and their location before and after calcination.

Table 1 displays the N_2 adsorption results of both samples after calcination. They showed a decrease in

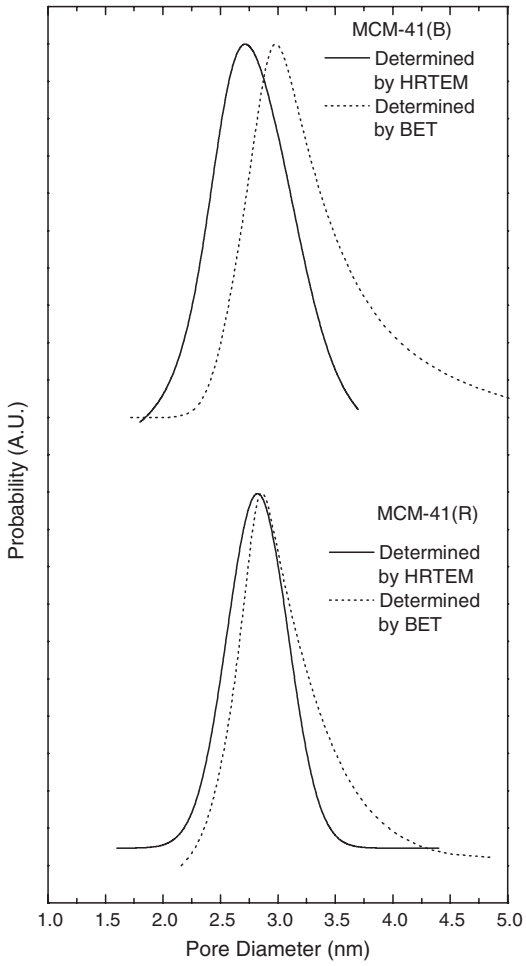

Fig. 5. Pore diameter distribution of the supports determined by HRTEM and BET.

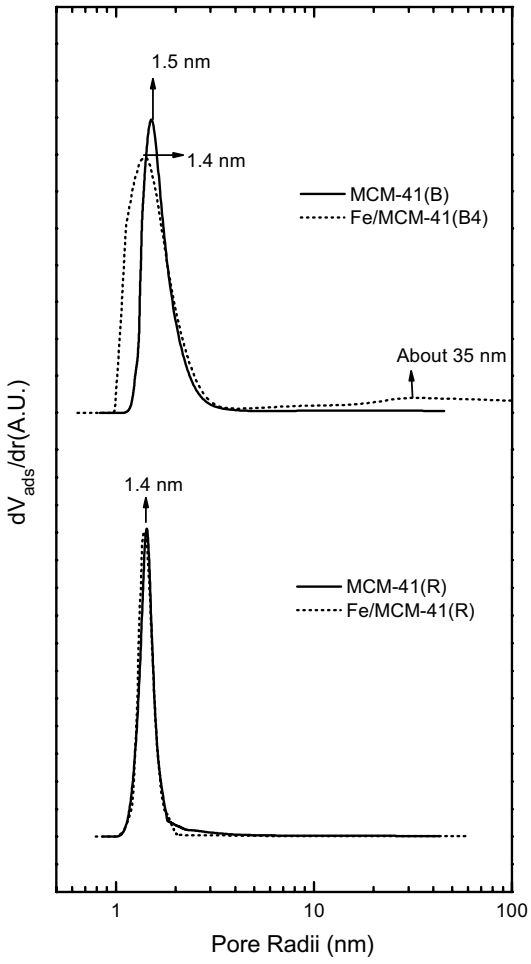

Fig. 6. Pore radii distribution of Fe/MCM-41(B4) and Fe/MCM-41(R) compared with their own supports.

their S_g compared with their own supports. Fig. 6 shows the pore radii distributions. Fe/MCM-41(B4) displays a broader and less intense distribution curve with a small displacement of the maximum compared to its support. The pore radii distribution of MCM-41(R) and Fe/MCM-41(R) after calcination are coincident (Fig. 6) while the pore-wall thickness increases from 1.4 to 1.9 nm (Table 1). Besides, a very broad and low intense peak, centered at about 35 nm can be seen in Fe/MCM-41(B4) after calcination. This fraction may be assigned to collapse of some walls that lead to the formation of channels with larger diameters.

Fig. 7 shows the Mössbauer spectra at 298 and 22 K of Fe/MCM-41(B4) before calcination and of Fe $(AcAc)_3$ for comparison. All spectra display only one singlet at both temperatures. The δ value for $Fe(AcAc)_3$ is similar to that found by Klinedinst and Boudart [9]. The resemblance between the spectra of $Fe(AcAc)_3$ and Fe/MCM-41(B4) at both temperatures suggests the maintenance of the salt structure in the impregnated sample. An increase of the electron density at the Fe^{3+} nucleus can be inferred from the δ decrease between

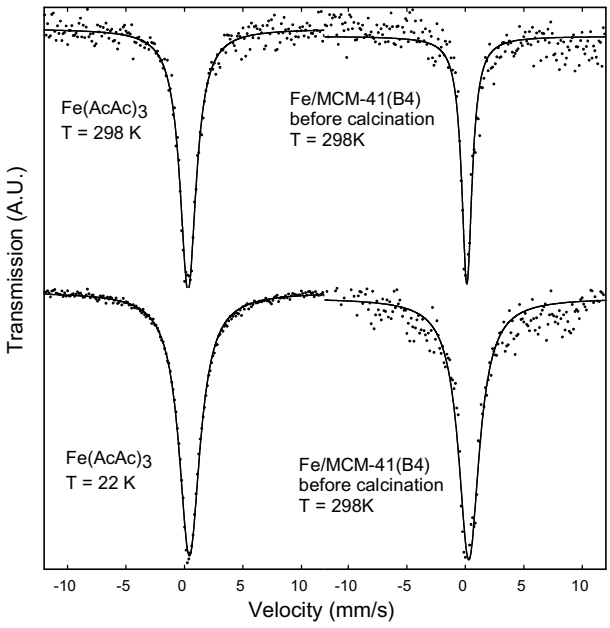

Fig. 7. Mössbauer spectra at 298 and 22 K of $Fe(AcAc)_3$, and Fe/MCM-41(B4) before calcination.

the samples (Table 2), that is likely originated in the salt-support interaction.

The Mössbauer spectra of Fe/MCM-41(B4) after calcination at 298 and 22 K shows an asymmetric doublet (Fig. 8). The hyperfine parameters obtained by fitting (Table 3) can be assigned to superparamagnetic crystals of Fe_2O_3 and/or paramagnetic exchanged Fe^{3+} ions. Since MCM-41(B) does not have exchangeable sites [10] and the impregnating solution is non-polar, we discard the existence of exchanged Fe^{3+}. It is remarkable that the spectrum background at 22 K is flat, suggesting that the magnetic ordering take place at a much lower temperature, evidencing the very small size of the iron oxide crystallites.

The absence of magnetic ordering in the Mössbauer signal does not allow to tell if the iron oxides is α-Fe_2O_3 or γ-Fe_2O_3. However, considering that the conditions of the $Fe(AcAc)_3$ decomposition used may produce γ-Fe_2O_3 [11], it is possible to estimate the upper limit of particle size assuming that this was the oxide obtained. Since, the blocking temperature is lower than 22 K, the Nèel-Brown model [12] can be used to estimate a value of 3.8 nm for the oxide particle diameter.

Fig. 8 also shows the Mössbauer spectra at 298 and 22 K of Fe/MCM-41(R). A doublet similar to that found for Fe/MCM-41(B4) after calcination appears at 298 K (Table 3). However, at 22 K the spectrum shows a magnetic splitting with a very intense central peak and four additional peaks. Two sextets and one singlet were used in fitting. The hyperfine parameters of the sextuplets (Table 3) were assigned to the "core" and "shell" signals of small α-Fe_2O_3 crystals [13–15].

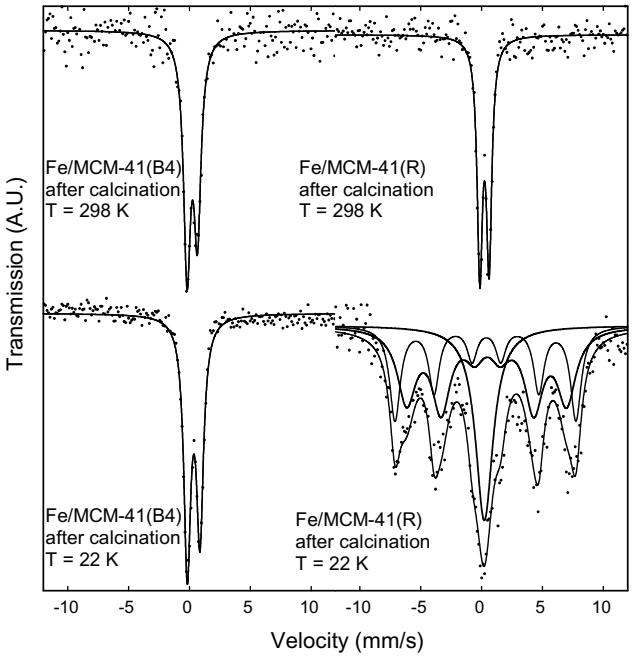

Fig. 8. Mössbauer spectra at 298 and 22 K of Fe/MCM-41(B4) and Fe/MCM-41(R), after calcination.

Using the population ratio of both sextets and assuming spherical and equal particles [13], an average diameter of 1.6 nm was obtained. The central signal was attributed to particles smaller than 1.6 nm that are still relaxing.

STEM-HAADF is a powerful method to distinguish the iron nanoparticles from the support since the contrast of the image is strongly correlated with the atomic

Table 2
Mössbauer hyperfine parameters at 298 and 22 K of the iron species in $Fe(AcAc)_3$ and Fe/MCM-41(B4) before calcinations

Samples	Parameters	T = 298 K	T = 22 K
$Fe(AcAc)_3$	δ (mm/s)	0.41 ± 0.01	0.53 ± 0.01
Fe/MCM-41(B4)	δ (mm/s)	0.24 ± 0.02	0.40 ± 0.02

δ: Isomer shift (all the isomer shifts are referred to α-Fe at 298 K).

Table 3
Mössbauer parameters of Fe/MCM-41(B4) and Fe/MCM-41(R) at 298 and 22 K after calcinations

Species	Parameter	Fe/MCM-41(B4) T = 298 K	Fe/MCM-41(B4) T = 22 K	Fe/MCM-41(R) T = 298 K	Fe/MCM-41(R) T = 22 K
Fe^{3+}	Δ (mm/s)	0.85 ± 0.02	1.04 ± 0.01	0.76 ± 0.01	–
	δ (mm/s)	0.34 ± 0.01	0.45 ± 0.01	0.34 ± 0.01	–
	%	100 ± 11	100 ± 4	100 ± 7	–
Fe^{3+}	δ (mm/s)	–	–	–	0.32 ± 0.03
	%	–	–	–	25 ± 4
"core"	H (T)	–	–	–	46.2 ± 0.4
α-Fe_2O_3	δ (mm/s)	–	–	–	0.46 ± 0.03
	2ε (mm/s)	–	–	–	−0.08 ± 0.06
	%	–	–	–	29 ± 8
"shell"	H (T)	–	–	–	40 ± 1
α-Fe_2O_3	δ (mm/s)	–	–	–	0.55 ± 0.04
	2ε (mm/s)	–	–	–	−0.07 ± 0.07
	%	–	–	–	46 ± 12

H: Hyperfine magnetic field in Teslas. δ: Isomer shift (all the isomer shifts are referred to α-Fe at 298 K). 2ε: Electrical quadrupole interaction. Δ: Quadrupole splitting.

number (Z-contrast imaging) and specimen thickness. STEM-HAADF images of Fe/MCM-41(R) are shown in Fig. 9. Contrast due to the MCM-41(R) symmetry is observed as well as brighter contrast corresponding to iron oxide species. The MCM-41(R) structure was clearly maintained after iron impregnation and calcination. The iron species were evidenced by the brighter contrast and were conclusively identified by EDS for individual nanoparticles like those marked with a circle in Figs. 10 and 11. Two different characteristic sizes of bright contrast from iron oxide particles are apparent. The small bright spots, some of them marked with white arrows (Fig. 9), have a size of the order of the pore size and would correspond to iron oxide located inside the pores. It is interesting to note that, when one channel is filled with iron oxide, the neighbors are empty. The other brighter areas, some of them marked with a rectangle in the micrographs (Fig. 9), give a smeared contrast extended over more than one channel, and would correspond to iron oxide particles on the external surface. Instead, we cannot detect any Fe oxide crystals in Fe/MCM-41(B4) by contrast due to the low structural regularity of the MCM-41(B) after the preparation steps.

Bearing in mind the HRTEM results and the Mössbauer size estimations we could infer that the major fraction of the iron oxide crystals could be located inside the channels in Fe/MCM-41(R). The opposite occurs for Fe/MCM-41(B4).

We can speculate that the hydrophylicity of the pore-walls would hinder the pore filling with the non-aqueous solution of the organic iron salt used.

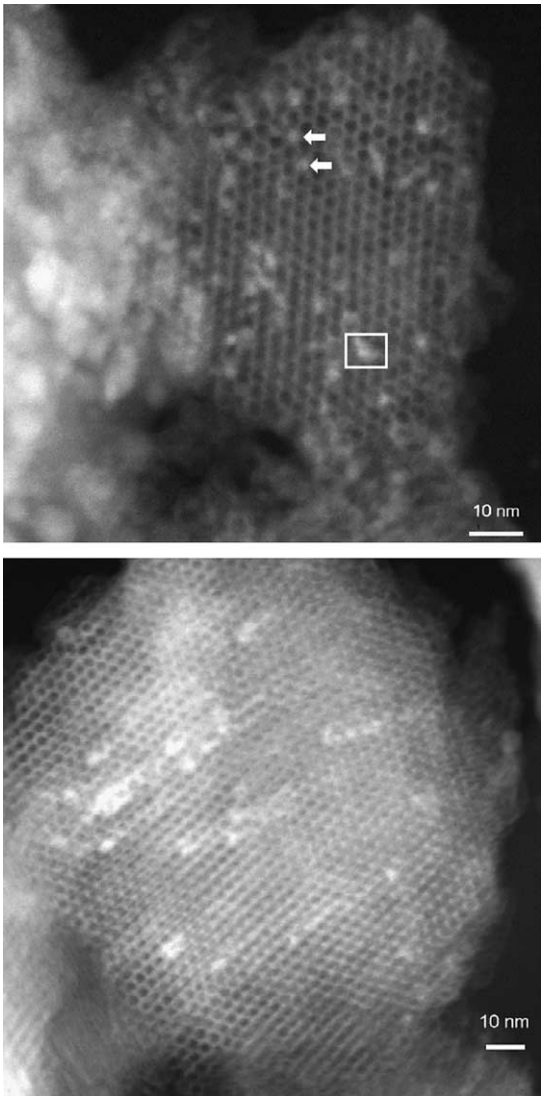

Fig. 9. STEM-HAADF images of Fe/MCM-41(R).

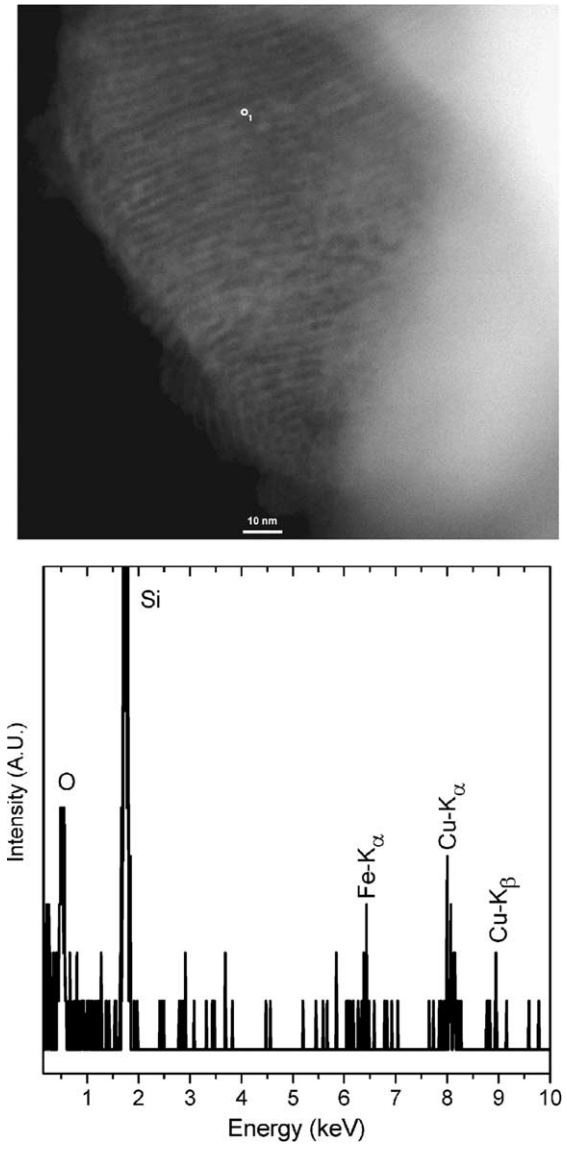

Fig. 10. STEM-HAADF image and EDS spectrum of the nanoparticle marked with a circle showing the presence of iron oxide crystals inside the Fe/MCM-41(R) channels.

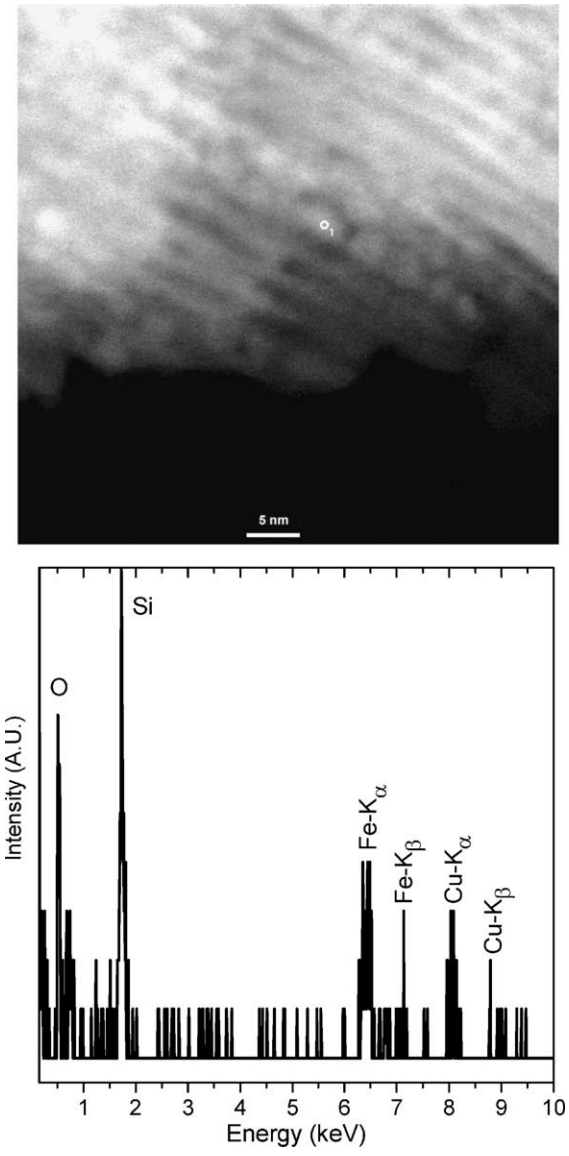

Fig. 11. STEM-HAADF image and EDS spectrum of the nanoparticle marked with a circle showing the presence of iron oxide crystals inside the Fe/MCM-41(R) channels.

4. Conclusions

We have found that the mesoporous solid MCM-41 can show different long range structural order and pore-wall thickness depending on the preparation method. Both properties are very important when the material is used as support for iron oxide nanoparticles.

MCM-41 synthesized without pH adjustment (MCM-41(B)) presents an imperfect arrangement and thin pore-wall thickness. Hence, just a small amount of water is enough to produce the structure collapse during the preparation steps. Therefore, to prepare Fe/MCM-41 using this support by PVI impregnation method it is necessary to dissolve an organic iron salt in a non-polar organic solvent. This condition prevents the iron ions to get into the channels. We believe that a functionalization of the silanols surface groups with silylating agents could solve this problem.

MCM-41 synthesized with pH adjustment during the synthesis process (MCM-41(R)) leads to a material with a more ordered structure and a thicker pore-wall thickness. These properties allow to obtain α-Fe_2O_3 nanocrystals inside the channels without structure loss when the support is impregnated with iron salt in aqueous solution by traditional methods. In addition, the α-Fe_2O_3 crystals exhibit a narrow size distribution with a small average crystal diameter of 1.6 nm.

Acknowledgements

The authors acknowledge the financial support of this work by CONICET, ANPCyT, UNLP and CICPBA.

M.S. Moreno acknowledges the partial financial support of CONICET-Argentina and the International Atomic Energy Agency (IAEA), and to Dr. P.A. Midgley at the Old Cavendish Laboratory (University of Cambridge, UK) for facilities and discussion on STEM-HAADF images.

References

[1] M. Boudart, A. Delbouille, J.A. Dumesic, S. Khammouma, H. Topsøe, J. Catal. 37 (1975) 486.
[2] M.A. Mc Donald, D.A. Storm, M. Boudart, J. Catal. 102 (1986) 386.
[3] T. Lin, Zeolite supported iron–cobalt catalyst for the Fischer-Tropsch synthesis, Ph.D. Northwestern University, 1984.
[4] S.G. Marchetti, M.V. Cagnoli, A.M. Alvarez, J.F. Bengoa, R.C. Mercader, A.A. Yeramián, Appl. Surf. Sci. 165 (2000) 91.
[5] J.S. Beck, J.C. Vartuli, W.J. Roth, M.E. Leonowicz, C.T. Kresge, K.D. Schmitt, C.T-W. Chu, D.H. Olson, E.W. Sheppard, S.B. Mc Cullen, J.B. Higgins, J.L. Schlenker, J. Am. Chem. Soc. 114 (1992) 10834.
[6] C. Noda Pérez, E. Moreno, C.A. Henriques, S. Valange, Z. Gabelica, J.L.F. Monteiro, Micropor. Mesopor. Mater. 41 (2000) 137.
[7] R. Ryoo, J.M. Kim, J. Chem. Soc., Chem. Commun. (1995) 711.
[8] M. Kruk, M. Jaroniec, R. Ryoo, J.M. Kim, Micropor. Mater. 12 (1997) 93.
[9] K.A. Klinedinst, M. Boudart, J. Catal. 28 (1973) 322.
[10] J.M. Kim, J.H. Kwak, S. Jun, R. Ryoo, J. Phys. Chem. 99 (1995) 16742.
[11] B. Pal, M. Sharon, Thin Solid Films 379 (2000) 83.
[12] W. Kündig, H. Bommel, G. Constabaris, R.H. Lindquist, Phys. Rev. 142 (1966) 327.
[13] M. Vazquez Mansilla, R.D. Zysler, C. Arciprete, M.I. Dimitrijewits, C. Saragovi, J.M. Greneche, J. Magn. Magn. Mater. 204 (1999) 29.
[14] M.V. Cagnoli, N.G. Gallegos, A.M. Alvarez, J.F. Bengoa, A.A. Yeramián, S.G. Marchetti, Stud. Surf. Sci. Catal. 135 (2001) 272.
[15] M.V. Cagnoli, N.G. Gallegos, A.A. Alvarez, J.F. Bengoa, A.A. Yeramián, M. Schmal, S.G. Marchetti, Appl. Catal. A: Gen. 5954 (2002) 1.